Robust Antiferromagnetism and Structural Disorder in $Bi_xCa_{1-x}FeO_3$ Perovskites

Wei-tin Chen,[†] Anthony J. Williams,[‡,†] Luis Ortega-San-Martin,[§,†] Ming Li,[||] Derek C. Sinclair,[||] Wuzong Zhou,[⊥] and J. Paul Attfield*,[†]

Centre for Science at Extreme Conditions and School of Chemistry, The University of Edinburgh, Edinburgh EH9 3JZ, United Kingdom, Department of Engineering Materials, The University of Sheffield, Sheffield S1 3JD, United Kingdom, and School of Chemistry, University of St. Andrews, St. Andrews KY16 9ST, United Kingdom

Received November 14, 2008. Revised Manuscript Received April 2, 2009

An investigation of Ca substitution in the multiferroic material $BiFeO_3$ shows that a wide range of perovskites $Bi_xCa_{1-x}FeO_3$ ($0.4 \leq x \leq 1.0$) can be prepared by sintering in air at 810−960 °C. $0.4 \leq x < 0.8$ samples are cubic $Pm\bar{3}m$, whereas $x = 0.8$ and 0.9 show a coexistence of the cubic and the rhombohedral $R3c$ $BiFeO_3$-type structure. Considerable disorder arising from Bi^{3+} lone-pair distortions is evidenced by synchrotron X-ray and neutron studies of the average structures of the cubic phases, and electron microscopy reveals commensurate and incommensurate local superstructures. The $Bi_xCa_{1-x}FeO_3$ ($0.4 \leq x \leq 1.0$) materials show a remarkably robust antiferromagnetic order with $T_N = 623-643$ K and ordered moments of 3.6−4.1 μ_B. They are "leaky" dielectrics with relative permittivities of ∼30−100 and bulk resistivities ∼50−500 kΩ cm at room temperature. The activation energy for bulk conduction increases from 0.27 eV for $x = 0.4$ to 0.5 eV for $x = 1$, but with a discontinuity at the cubic-rhombohedral boundary. Further processing of the $x = 0.8$ and 0.9 compositions to reduce conductivity through control of oxygen content could lead to improved $BiFeO_3$-based multiferroics.

1. Introduction

Perovskite-type transition metal oxides ABO_3 are of great interest because of their magnetic, dielectric, and transport properties that emerge from the coupling of spin, charge, and orbital degrees of freedom.[1] Ferromagnetism and ferroelectricity are two particularly useful properties but these do not often occur simultaneously in perovskites. "Multiferroic" properties can arise, however, when a polar cation such as Bi^{3+} or Pb^{2+} is present in the A-site of the perovskite and a magnetic cation is at the B-site.[2] The off-center "lone pair" A-cation displacement may lead to polar superstructures with appreciable ferroelectricity, whereas ferro- or antiferromagnetic coupling of the transition metal cation spins leads to long-range magnetic order.

$BiFeO_3$ and $BiMnO_3$ both show multiferroic properties.[3−6] $BiMnO_3$ is a monoclinically distorted perovskite with a structural phase transition to tetragonal symmetry at 760 K[7] and is ferroelectric below 450 K.[8] The ferroelectricity persists to low temperatures through the ferromagnetic transition at 105 K.[6,9,10] Spin, charge, and orbital order have been studied extensively in strontium-[10,11] and calcium-substituted[12,13] bismuth manganites.

$BiFeO_3$ has a rhombohedrally distorted acentric structure (space group $R3c$), and shows G-type antiferromagnetic order with a long-periodicity spiral below the Néel temperature of 643 K and ferroelectricity below 1103 K. The ferroelectricity of $BiFeO_3$ is due to Bi^{3+} $6s^2$ lone-pair distortions, whereas the residual moment of the canted Fe^{3+} spin structure results in weak ferromagnetism.[4] A-site substitutions of trivalent (La^{3+}, Nd^{3+}, or Sm^{3+})[14−19] or divalent (Ba^{2+}, Pb^{2+},

* Corresponding author. E-mail: j.p.attfield@ed.ac.uk.
[†] The University of Edinburgh.
[‡] New address: Department of Chemistry and Materials Institute, Princeton University, Princeton, NJ 08544.
[§] New address: Instituto de Ciencia de Materiales de Aragón, ICMA, CSIC-Universidad de Zaragoza, 50018-Zaragoza, Spain.
[||] The University of Sheffield.
[⊥] University of St. Andrews.

(1) Goodenough, J. B. *Rep. Prog. Phys.* **2004**, *67*, 1915–1993.
(2) Khomskii, D. I. *J. Magn. Magn. Mater.* **2006**, *306*, 1–8.
(3) Blaauw, C.; Woude, F. v. d. *J. Phys. C: Solid State Phys.* **1973**, *6*, 1422–1431.
(4) Fischer, P.; Polomska, M.; Sosnowska, I.; Szymanski, M. *J. Phys. C: Solid State Phys.* **1980**, *13*, 1931–1940.
(5) Sosnowska, I.; Neumaier, T. P.; Steichele, E. *J. Phys. C: Solid State Phys.* **1982**, *15*, 4835–4846.
(6) Sugawara, F.; Iiida, S.; Syono, Y.; Akimoto, S.-i. *J. Phys. Soc. Jpn.* **1968**, *25*, 1553−1558.
(7) Faqir, H.; Chiba, H.; Kikuchi, M.; Syono, Y.; Mansori, M.; Satre, P.; Sebaoun, A. *J. Solid State Chem.* **1999**, *142*, 113–119.
(8) Moreira dos Santos, A.; Parashar, S.; Raju, A. R.; Zhao, Y. S.; Cheetham, A. K.; Rao, C. N. R. *Solid State Commun.* **2002**, *122*, 49–52.
(9) Bokov, V. A.; Myl'nikova, I. E.; Kizhaev, S. A.; Bryzhina, M. F.; Grigoryan, N. A. *Sov. Phys.-Solid State* **1966**, *7*, 2993–2994.
(10) Chiba, H.; Atou, T.; Syono, Y. *J. Solid State Chem.* **1997**, *132*, 139–143.
(11) Goff, R. J.; Attfield, J. P. *J. Solid State Chem.* **2006**, *179*, 1369–1374.
(12) Chiba, H.; Kikuchi, M.; Kusaba, K.; Muraoka, Y.; Syono, Y. *Solid State Commun.* **1996**, *99*, 499–502.
(13) Troyanchuk, I. O.; Mantytskaya, O. S.; Chobot, A. N. *Phys. Solid State* **2002**, *44*, 2266–2270.
(14) Zhang, S.-T.; Pang, L.-H.; Zhang, Y.; Lu, M.-H.; Chen, Y.-F. *J. Appl. Phys.* **2006**, *100*, 114108.
(15) Yuan, G. L.; Or, S. W.; Chan, H. L. W. *J. Phys. D: Appl. Phys.* **2007**, *40*, 1196–1200.
(16) Mathe, V. L.; Patankar, K. K.; Patil, R. N.; Lokhande, C. D. *J. Magn. Magn. Mater.* **2004**, *270*, 380–388.
(17) Yuan, G. L.; Or, S. W.; Liu, J. M.; Liu, Z. G. *Appl. Phys. Lett.* **2006**, *89*, 052905.

10.1021/cm8031048 CCC: $40.75
Published on Web 04/27/2009

Sr^{2+}, or Ca^{2+})[20−23] cations for Bi^{3+} and B-sublattice dopings with V^{5+}, Nb^{5+}, Mn^{4+}, Ti^{4+}, or Cr^{3+} have recently been investigated in order to improve the magnetoelectric properties.[24−29]

Solid solutions of $BiFeO_3$ with $CaFeO_3$ or $SrFeO_3$ are of interest as these perovskites also have notable properties, although high oxygen pressures are required to synthesize stoichiometric materials. $SrFeO_3$ has a cubic perovskite structure and is antiferromagnetically ordered below 130 K,[30,31] whereas $CaFeO_3$ has a $GdFeO_3$-type orthorhombic perovskite structure and shows charge disproportionation below 290 K and antiferromagnetic order at 116 K.[32] An extensive range of $Bi_xSr_{1-x}FeO_3$ solid solution ($x = 0.33-0.80$) has been reported.[21] These materials are cubic perovskites and show weak ferromagnetism. In the $Bi_xCa_{1-x}FeO_3$ system, weak ferromagnetism was observed at small Ca-dopings ($x = 0.9$ and 0.95),[23] and a study of $Bi_{0.8}Ca_{0.2}FeO_3$ was recently reported,[22] but no systematic study of the series has been presented. Here we report the preparation, structural and physical properties of $Bi_xCa_{1-x}FeO_3$ materials in the range $0.4 \leq x \leq 1.0$.

2. Experimental Section

$Bi_xCa_{1-x}FeO_3$ materials were prepared by high-temperature solid-state reactions in air. Initials attempts to prepare $x = 0.0$ and 0.2 samples gave mixtures of brownmillerite ($Ca_2Fe_2O_5$) and perovskite phases, but single-phase perovskites were obtained for $x \geq 0.4$. Ten gram samples with $x = 0.4$, 0.5, 0.6, 0.67, 0.8, 0.9, and 1.0 were prepared from stoichiometric amounts of Bi_2O_3, Fe_2O_3, and $CaCO_3$ (all Aldrich, >99.9% pure). The reactants were ground and mixed into a fine homogeneous powder which was pressed into pellets. The pellets were loaded in an alumina boat and heated at 5 °C/min. to a temperature appropriate for sintering without melting. The $x = 1.0$ sample was calcined at 810 °C for one hour, whereas $x = 0.9-0.4$ samples were calcined for 72 h at temperatures increasing from 900 to 960 °C. To obtain well-crystallized products, we furnace-cooled the $x = 1.0$ and 0.9 samples at ~5 °C/min, but the $x = 0.8$, 0.67, 0.6, 0.5, and 0.4 samples were quenched to room temperature to prevent formation of the brownmillerite phase. The pellets were then ground, repressed, and calcined several times to complete the reaction until phase-pure samples were confirmed by X-ray powder diffraction.

Laboratory X-ray powder diffraction data were collected in the range $15° \leq 2\theta \leq 60°$ with an integration time of 2 s per 0.007 ° step using a Bruker D8 Advance diffractometer with Ge (111) monochromated Cu $K\alpha_1$ radiation ($\lambda = 1.540598$ Å) at room temperature. High-resolution synchrotron X-ray diffraction data from samples in 0.3 and 0.7 mm diameter capillaries were collected on instruments ID31 and BM01B, respectively, at the ESRF, Grenoble. ID31 data were collected with a wavelength of 0.39825 Å in the angular range $3° \leq 2\theta \leq 30°$ from $x = 0.4-1.0$ samples at room temperature and for $x = 0.6$, 0.67, 0.8 materials at high temperatures. High-temperature data from BM01B in 50 °C steps up to 400 °C were collected with wavelength 0.50010 Å in the range $1° \leq 2\theta \leq 30°$, counting for 3 h for each pattern.

Neutron powder diffraction data from polycrystalline samples in 8 mm diameter vanadium cans were collected on instruments Super-D2B and D1B at the ILL, Grenoble, France. Super-D2B data were recorded at 10 and 300 K. Data were collected in the angular range $5° \leq 2\theta \leq 155°$ for 50 min per scan with a neutron wavelength of 1.594 Å. High-temperature neutron powder diffraction data were collected on instrument D1B using a 2.52 Å neutron wavelength. Data were recorded in 1 °C steps from room temperature to 400 °C in the angular range $5° \leq 2\theta \leq 85°$ at a 0.8 °C/min. ramping rate, counting for 1.25 min per scan. The X-ray and neutron diffraction data were analyzed by the Rietveld method[33] using the GSAS software package.[34]

Selected area electron diffraction (SAED) patterns and high-resolution transmission electron microscopic (HRTEM) images of $Bi_{0.8}Ca_{0.2}FeO_3$ and $Bi_{0.67}Ca_{0.33}FeO_3$ samples were collected on a JEOL JEM 2011 electron microscope at room temperature. For transmission electron microscopy, a small amount of the sample powder was mounted on a copper grid with a holey carbon film.

DC magnetization data were collected from a Quantum Design MPMS SQUID magnetometer for 5−300 K in an applied field of 10 kOe under field-cooling (FC) and zero-field-cooling (ZFC) conditions. Magnetisation loops were measured at 5 K in fields between −10 and 10 kOe.

The dielectric properties of ceramic samples were investigated over the frequency range 1×10^0 to 1×10^6 Hz using an impedance analyzer (model E4980A, Agilent, USA) with an applied voltage of 100 mV and Au sputtered electrodes. Low-temperature measurements (10−320 K) were performed in an Oxford Cryocooler (model CC 1.5 Oxford Instruments, Oxfordshire, U.K.). All data were corrected for sample geometry and analyzed using the commercial software package Z-View (Scribner Associates, Inc., Charlottesville, VA, version 2.9c).

3. Results

3.1. Phase Formation. $Bi_xCa_{1-x}FeO_3$ solid solutions in the range $0.4 \leq x \leq 1.0$ were prepared by high-temperature solid-state reactions in air. Solid-solution formation is evident from the laboratory X-ray powder diffraction patterns shown in Figure 1, as the lattice contracts with decreasing x. The conditions needed to prepare materials that are single phase

(18) Mathe, V. L. *J. Magn. Magn. Mater.* **2003**, *263*, 344–352.
(19) Yuan, G. L.; Or, S. W. *J. Appl. Phys.* **2006**, *100*, 024109.
(20) Wang, D. H.; Goh, W. C.; Ning, M.; Ong, C. K. *Appl. Phys. Lett.* **2006**, *88*, 212907.
(21) Li, J.; Duan, Y.; He, H.; Song, D. *J. Alloys Compd.* **2001**, *315*, 259–264.
(22) Khomchenko, V. A.; Kiselev, D. A.; Vieira, J. M.; Kholkin, A. L.; Sa, M. A.; Pogorelov, Y. G. *Appl. Phys. Lett.* **2007**, *90*, 242901.
(23) Kothari, D.; Reddy, V. R.; Gupta, A.; Sathe, V.; Banerjee, A.; Gupta, S. M.; Awasthi, A. M. *Appl. Phys. Lett.* **2007**, *91*, 202505.
(24) Yu, B.; Li, M.; Liu, J.; Guo, D.; Pei, L.; Zhao, X. *J. Phys. D: Appl. Phys.* **2008**, *41*, 065003.
(25) Jun, Y.-K.; Moon, W.-T.; Chang, C.-M.; Kim, H.-S.; Ryu, H. S.; Kim, J. W.; Kim, K. H.; Hong, S.-H. *Solid State Commun.* **2005**, *135*, 133–137.
(26) Yang, C. H.; Koo, T. Y.; Jeong, Y. H. *Solid State Commun.* **2005**, *134*, 299–301.
(27) Santos, I. A.; Grande, H. L. C.; Freitas, V. F.; de Medeiros, S. N.; Paesano, J. A.; Cótica, L. F.; Radovanovic, E. *J. Non-Cryst. Solids* **2006**, *352*, 3721–3724.
(28) Qi, X.; Dho, J.; Tomov, R.; Blamire, M. G.; MacManus-Driscoll, J. L. *Appl. Phys. Lett.* **2005**, *86*, 062903.
(29) Suchomel, M. R.; Thomas, C. I.; Allix, M.; Rosseinsky, M. J.; Fogg, A. M.; Thomas, M. F. *Appl. Phys. Lett.* **2007**, *90*, 112909.
(30) MacChesney, J. B.; Sherwood, R. C.; Potter, J. F. *J. Chem. Phys.* **1965**, *43*, 1907–1913.
(31) Adler, P.; Lebon, A.; Damljanovic, V.; Ulrich, C.; Bernhard, C.; Boris, A. V.; Maljuk, A.; Lin, C. T.; Keimer, B. *Phys. Rev. B: Condens. Matter Mater. Phys.* **2006**, *73*, 094451.
(32) Woodward, P. M.; Cox, D. E.; Moshopoulou, E.; Sleight, A. W.; Morimoto, S. *Phys. Rev. B: Condens. Matter Mater. Phys.* **2000**, *62*, 844–855.
(33) Rietveld, H. M. *J. Appl. Crystallogr.* **1969**, *2*, 65–71.
(34) Larson, A. C.; Dreele, R. B. V. *General Structure Analysis System (GSAS)*; Report LAUR 86-748; Los Alamos National Laboratory: Los Alamos, NM, 2004.

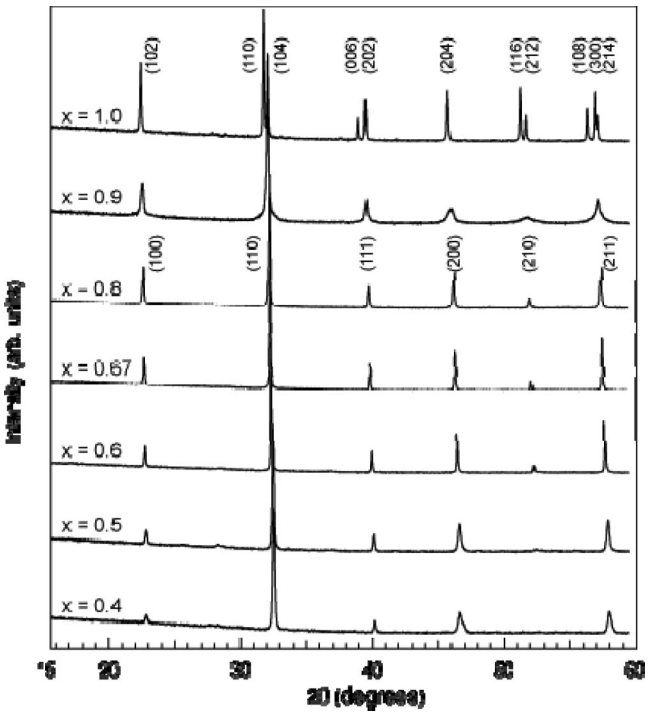

Figure 1. Laboratory X-ray diffraction patterns of $Bi_xCa_{1-x}FeO_3$ for $x = 0.4-1.0$ at room temperature with rhombohedral (for $x = 1.0$) and cubic (for $x = 0.8$) indexings shown.

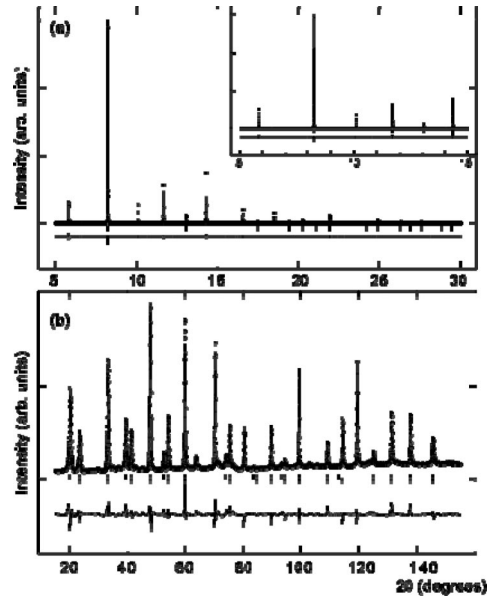

Figure 2. Fits of the disordered cubic $Pm\bar{3}m$ model for $Bi_{0.67}Ca_{0.33}FeO_3$ to (a) the room temperature ID31 synchrotron diffraction data and (b) the room temperature Super-D2B neutron diffraction data, where the upper and lower reflection markers correspond to the magnetic and nuclear phases, respectively.

by X-ray diffraction varied across the series. Furnace-cooling the Bi-rich $x = 1.0$ and 0.9 samples was found to give better-crystallized products, although the $x = 0.9$ peaks are broad as a result of the phase separation described below. By contrast, $0.4 \leq x \leq 0.8$ samples were quenched to room temperature as slow cooling resulted in the formation of the brownmillerite phase $Ca_2Fe_2O_5$. The peak broadening for the $x = 0.4$ sample shows that it is close to the solid solution limit; mixtures of perovskite and brownmillerite phases were obtained at lower x.

Attempts to obtain reliable thermogravimetric oxygen contents by hydrogen reduction were unsuccessful. The $Bi_xCa_{1-x}FeO_3$ materials are reduced to mixtures of Fe and (volatile) Bi metals and a brownmillerite phase, without a well-defined oxygen end point.

3.2. Crystal Structures. $BiFeO_3$ is a rhombohedrally distorted perovskite with a $\sqrt{2} \times \sqrt{2} \times 2\sqrt{3}$ $R3c$ supercell, in the hexagonal setting, of the primitive cubic perovskite cell. Rhombohedral peak splittings or broadenings are evident in the laboratory X-ray powder diffraction patterns (Figure 1) for the $x = 0.9$ and 1.0 samples, which were fitted by the $R3c$ model, while the $x = 0.4$, 0.5, 0.6, 0.67, and 0.8 patterns were all well-fitted by the cubic aristotype structure in space group $Pm\bar{3}m$.

Synchrotron powder X-ray data for the cubic phases (e.g., $x = 0.67$ in Figure 2a) show single sharp peaks, indicating that the samples are homogeneous, single-phase materials. However, the initial fits to the X-ray, and in particular, the nuclear peaks of the Super-D2B neutron powder diffraction patterns, were very poor. The ideal cubic perovskite structure was found to give very poor fits to the nuclear peaks of the Super-D2B neutron powder diffraction patterns of the $x = 0.4-0.8$ samples. No splittings or superlattice peaks (except those from the magnetic superstructure described later) were observed, and attempts to fit rhombohedral and other perovskite superstructures were unsuccessful. The further absence of any superstructure or structural anomalies for the $x = 0.67$ sample shows that long-range charge order is also absent. Greatly improved fits to the neutron data were obtained by introducing positional disorder into the cubic perovskite model. The A cations were refined on $(1/2 - x, 1/2 - x, 1/2 - x)$ to allow for [111] off-center displacements, while oxygen was fitted as $(1/2, y, y)$ to allow for local bending of the Fe−O−Fe bridges. Large values of the Bi:$x \approx 0.05$ and O:$y \approx 0.08$ shifts were observed. No evidence of significant oxygen deficiency was found within occupancy error limits of 1−2% allowed by these refinements.

Subtle peak splittings and shoulders in the high resolution synchrotron X-ray profile of $Bi_{0.8}Ca_{0.2}FeO_3$ at room temperature showed that two phases are present, so both cubic and rhombohedral phases were fitted to synchrotron and neutron patterns. The same procedure was used for the $x = 0.9$ sample, which shows very broad perovskite peaks.

The coordinates and derived results are shown in Tables 1 and 2, and the Rietveld fits to the room temperature synchrotron and neutron diffraction data of $Bi_{0.67}Ca_{0.33}FeO_3$, are shown in Figure 2. Although the fits to the neutron data are acceptable, the high χ^2 values and residual intensity differences observed in the profiles indicate that the disordered cubic model is only a first approximation to the complex local microstructures observed by HRTEM (see later), and diffuse background scattering features evidence further short-range order. Independently fitting the same disordered cubic model gives good fits to the synchrotron intensities (which are less sensitive to the oxygen distribution) with similar values of the Bi:x and O:y shifts, as shown in Table 1. This confirms that the disorder cubic model is an appropriate average description. The agreement

Table 1. Refinement Results for $Bi_xCa_{1-x}FeO_3$ Fitting Disordered Cubic and Rhombohedral Models to Room Temperature ID31 X-ray (bold font) and Super-D2B neutron data[a]

	x								
	0.4	0.5	0.6	0.67	0.8 C	0.8 R	0.9 C	0.9 R	1.0
a (Å)	**3.89012(5)**	**3.99917(3)**	**3.916436(4)**	**3.909564(5)**	**3.92158(2)**	**5.53921(4)**	**3.9401(1)**	**5.5546(4)**	**5.58000(1)**
	3.8889(1)	3.8980(1)	3.91531(5)	3.90851(5)	3.91912(7)	5.54134(9)	3.9357(4)	5.56694(11)	5.58418(1)
c (Å)						**13.57981(22)**		**13.7707(19)**	**13.87252(3)**
						13.5933(17)		13.7581(22)	13.8822(2)
V/f.u.(Å^3)	**58.869(2)**	**59.281(1)**	**59.756(1)**	**60.072(1)**	**60.309(1)**	**60.141(1)**	**61.166(7)**	**61.148(6)**	**62.345(3)**
	58.815(6)	59.228(5)	59.708(2)	60.020(2)	60.196(3)	60.247(9)	60.964(20)	61.542(12)	62.483(1)
phase fraction (%)					**59.3**	**40.7**	49.7	50.3	
					58.6	41.4	22.0	78.0	
Bi/Ca *x*	**0.4457(7)**	**0.4486(6)**	**0.4594(9)**	**0.4585(10)**	**0.4569(4)**		**0.4368(3)**		
	0.4479(14)	0.4568(34)	0.4556(21)	0.4554(22)	0.4880(87)		0.4586(18)		
U_{iso} (Å^2)	**0.0058(16)**	**0.0114(13)**	**0.0272(17)**	**0.0302(14)**	**0.0306(3)**				**0.0069(1)**
	0.0078(33)	0.0057(1)	0.0041(1)	0.0181(40)	0.0407(23)		0.0036(11)		0.0048(4)
Fe *z*						**0.2514(12)**		**0.2251(3)**	**0.22080(9)**
						0.2511(14)		0.2217(3)	0.2792(1)
U_{iso} (Å^2)	**0.0208(5)**	**0.0127(4)**	**0.0170(3)**	**0.0155(2)**	**0.0087(2)**				**0.0047(3)**
	0.0175(5)	0.0060(4)	0.0082(3)	0.0066(3)	0.0072(2)		0.0072(7)		0.0022(3)
m_z (μ_B)	3.645(31)	3.684(35)	3.731(33)	3.794(33)	3.904(37)		3.940(33)		4.104(28)
O *x*						**0.4162(17)**		**0.4226(42)**	**0.4371(11)**
						0.4267(14)		0.4423(9)	0.4275(3)
O *y*	**0.0811(10)**	**0.0855(9)**	**0.0765(6)**	**0.0767(8)**	**0.0767(10)**	**−0.0503(30)**	**0.0712(22)**	**0.0392(36)**	**0.0182(12)**
	0.0806(5)	0.0782(5)	0.0756(4)	0.0751(4)	0.0732(5)	0.0245(19)	0.0729(12)	0.0160(9)	−0.0194(3)
O *z*						**1.0198(13)**		**0.9608(13)**	**0.9495(4)**
						0.9835(17)		0.9554(5)	1.0484(1)
U_{iso} (Å^2)	**0.159(21)**	**0.0286(19)**	**0.0341(18)**	**0.0297(13)**	**0.0138(10)**				**0.0162(14)**
	0.0370(10)	0.0010(1)	0.0323(9)	0.0317(9)	0.0225(7)		0.0028(5)		0.0046(3)
R_{wp} (%)	**15.73**	**12.90**	**11.41**	**8.99**	**7.40**		**13.93**		**16.97**
χ^2	**5.157**	**5.138**	**1.697**	**1.709**	**1.878**		**6.326**		**5.885**
R_{wp} (%)	8.47	9.13	9.27	8.85	7.38		8.53		7.61
χ^2	6.457	6.409	7.727	7.211	4.630		6.074		4.072

[a] Both cubic (C) and rhombohedral (R) phases were used for $x = 0.8$ and 0.9 samples. Lattice parameters, atomic positions, isotropic temperature factors, magnetic moments, phase fractions (for $x = 0.8$ and 0.9 samples), R-factors, and χ^2 are listed. For the disordered cubic model, atom positions are Bi/Ca, 8(g), $(1/2 - x, 1/2 - x, 1/2 - x)$; Fe, 1(a), (0, 0, 0); O, 12(j), (1/2, *y*, *y*) in space group $Pm\bar{3}m$ (No. 221). Rhombohedral atom positions are Bi/Ca, 6(a), (0, 0, $z = 0$); Fe, 6(a), (0, 0, *z*); O, 18(b), (*x*, *y*, *z*) in space group *R*3*c* (No. 161).

between the cubic:rhombohedral phase ratios (both 59:41) from the X-ray and neutron fits to the $x = 0.8$ data shows that the two phase model is realistic. However, the same procedure gives very different ratios for the X-ray (50:50) and neutron (22:78) fits for $x = 0.9$, showing that this structural description is less precise, perhaps because of the formation of a continuum of structures.

The variations in lattice constant and unit-cell volumes with *x* are shown in Figure 3. The expansion of the cell with *x* is expected, as Bi^{3+} and Fe^{3+} are respectively larger than Ca^{2+} and Fe^{4+}. A change from rhombohedral to cubic symmetry at $x = 0.8$ is also observed in the $Bi_xSr_{1-x}FeO_3$ phase diagram.[21] However, it is not clear whether substantial local disorder is also present in the cubic $Bi_xSr_{1-x}FeO_3$ samples with $x = 0.33-0.8$.

Variable-temperature synchrotron X-ray powder diffraction data were collected from the $x = 0.6$, 0.67, and 0.8 $Bi_xCa_{1-x}FeO_3$ samples from room temperature to 400 °C. The $Bi_{0.8}Ca_{0.2}FeO_3$ sample, which was prepared by quenching from 950 °C, contains 59% cubic and 41% rhombohedral phases at room temperature. On heating, the fraction of the cubic phase decreased to 45% at 250 °C, and then dropped to 5% at 350 °C, as shown in Figure 4. Above 350 °C, the sample underwent an irreversible chemical phase separation into two perovskite-like phases. These observations demonstrate the relative metastabilities of the two components. Initial heating enables the disordered cubic phase to relax and order into the rhombohedral superstructure through a displacive transition. However, further heating leads to an irreversible reconstructive change into an equilibrium mixture of several phases. The high temperature behavior of the $x = 0.6$ and 0.67 samples was also investigated, but for these materials a straightforward thermal expansion of the cubic phase was observed with no relaxation to the rhombohedral structure.

3.3. Transmission Electron Microscopy. Although the $Bi_xCa_{1-x}FeO_3$ materials are disordered solid solutions by the above bulk structure analyses, the large atom shifts originating from the different sizes and coordination environments of Ca^{2+} and Bi^{3+} is expected to lead to complex local superstructures, as observed previously in similar oxide materials.[35−37] An initial investigation of the $x = 0.67$ and 0.8 samples demonstrates that substantial local order occurs (Figures 5 and 6). In $Bi_{0.67}Ca_{0.33}FeO_3$, a dominant 5-fold superstructure is observed along the cubic-[100] direction (Figure 5a). In many crystallites, this superstructure appears in both [100] and [010] zone axes, forming a domain structure as shown in Figure 5b.

$Bi_{0.8}Ca_{0.2}FeO_3$ presents more complex superstructures, in keeping with the coexistence of bulk cubic and rhombohedral phases. Figure 6 shows that an 8-fold commensurate superstructure is seen along the [100] and [010] directions, again indicating a domain structure, which is confirmed by

(35) Zhou, W.; Jefferson, D. A.; Thomas, J. M. *Proc. R. Soc. London, Ser. A* **1986**, *406*, 173–182.
(36) Zhou, W. *J. Solid State Chem.* **1988**, *76*, 290–300.
(37) Zhou, W. *J. Solid State Chem.* **1992**, *101*, 1–17.

Table 2. Metal to Oxygen Bond Distances (Å) and O−Fe−O Angles (deg) for $Bi_xCa_{1-x}FeO_3$ in Disordered Cubic and Rhombohedral Structures, from the fits to D2B data in Table 1[a]

	x								
	0.4	0.5	0.6	0.67	0.8 C	0.8 R	0.9 C	0.9 R	1.0
Bi/Ca−O	2.030(8)−3.485(9)	2.093(18)−3.430(20)	2.109(12)−3.430(13)	2.111(12)−3.438(13)	2.30(5)−3.24(5)	3.061(18) × 3	2.154(12)−3.423(13)	3.209(3) × 3	3.215(1) × 3
						2.567(8) × 3		2.495(5) × 3	2.534(1) × 3
						2.311(8) × 3		2.302(6) × 3	2.263(2) × 3
						3.254(7) × 3		3.378(6) × 3	3.457(2) × 3
Fe−O	1.9944(6)	1.9961(6)	1.9978(5)	2.0019(5)	2.0011(6)	2.073(12) × 3	2.0091(13)	2.086(4) × 3	2.110(2) × 3
						1.994(12) × 3		1.955(4) × 3	1.956(2) × 3
O−Fe−O	70.7(1)−109.4(1)	71.2(1)−108.8(1)	72.0(1)−108.0(1)	71.9(1)−108.1(1)	72.5(1)−107.5(1)	81.0(4) × 3	72.6(3)−107.4(3)	81.6(2) × 3	79.5(1) × 3
						165.2(5) × 3		167.1(3) × 3	164.6(1) × 3
	154.3(2)−180	155.1(2)−180	156.0(1)−180	155.9(1)−180	156.6(2)−180	89.2(2) × 3	156.7(4)−180	89.4(1) × 3	89.6(1) × 3
						86.5(1) × 3		88.0(1) × 3	88.0(1) × 3
						101.4(4) × 3		99.5(2) × 3	100.9(1) × 3

[a] Ranges of some distances and angles are shown for the disordered cubic $Pm\bar{3}m$ mode.

Figure 3. (a) Variations in lattice parameters and volume with *x* for the cubic (C-subscripts) and rhombohedral (R) phases in the $Bi_xCa_{1-x}FeO_3$ series, from fits to ID31 synchrotron diffraction data.

Figure 4. Evolution of the lattice parameters and cubic phase fraction with temperature for the $Bi_{0.8}Ca_{0.2}FeO_3$ sample from fits to ID31 synchrotron diffraction data.

HRTEM images (Figure 5d). However, an incommensurate superstructure along [$\bar{1}$10] was observed from another SAED pattern (Figure 6b) and the corresponding HRTEM image is shown in Figure 5c. Some particles contained a 2-fold superstructure on the [100] zone axis (Figure 6c), whereas others had poor ordering as shown by the diffuse diffraction peaks along the [010] direction (Figure 6d).

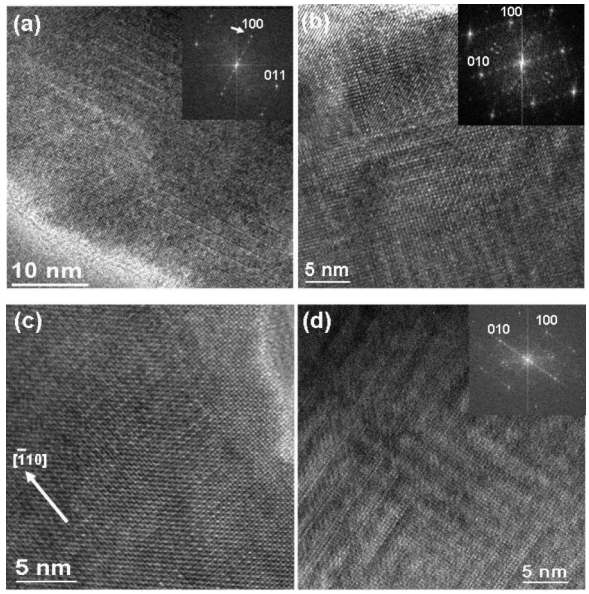

Figure 5. HRTEM images from (a, b) $Bi_{0.67}Ca_{0.33}FeO_3$ and (c, d) $Bi_{0.8}Ca_{0.2}FeO_3$, viewed down the (a) [01$\bar{1}$] and (b−d) [001] zone axes of the perovskite-type basic unit cells, showing several superstructures. The insets in a, b, and d show the corresponding FFT diffraction patterns.

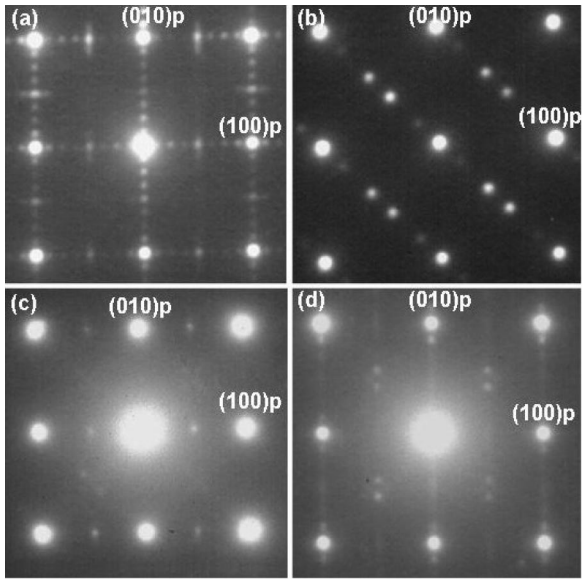

Figure 6. SAED patterns on the [001] projection of the perovskite-type basic unit cell from the $Bi_{0.8}Ca_{0.2}FeO_3$ sample, showing various superstructures.

Initial simulations suggest that the superstructures in $Bi_{0.67}Ca_{0.33}FeO_3$ and $Bi_{0.8}Ca_{0.2}FeO_3$ arise mainly from local Ca^{2+}/Bi^{3+} cation order accompanied by order of oxygen displacements, but further work on these and other samples will be needed to understand the detailed local structures of the $Bi_xCa_{1-x}FeO_3$ system.

3.4. Magnetic Properties. The magnetic properties of the $Bi_xCa_{1-x}FeO_3$ system have been investigated by magnetization measurements and neutron diffraction. Magnetic susceptibilities and $M-H$ loops are shown Figure 7. All of the samples show an almost flat susceptibility variation, confirming the results below from neutron data that they are antiferromagnetically ordered at and below room temperature. The $x = 0.8-1.0$ samples show a small net magnetization (largest saturated magnetization of $\sim 0.001\ \mu_B$ for $x =$ 0.9), which is consistent with some canting in the acentric rhombohedral phases observed above in this composition range. The cubic $x = 0.4-0.67$ phases have a linear $M-H$ response except for the $x = 0.6$ sample, which shows a small anomalous magnetization at low temperatures (see Figure 7b inset). This most probably evidence a small ferromagnetic impurity phase such as $Ca_2Fe_2O_5$, although why this is only apparent in the $x = 0.6$ sample is unclear.

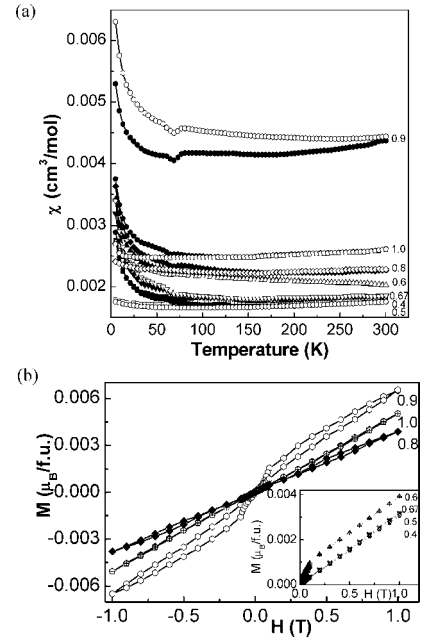

Figure 7. Magnetization measurements for $Bi_xCa_{1-x}FeO_3$: (a) variable-temperature ZFC and FC data (closed and open symbols, respectively) measured in a field of $H = 10$ kOe; (b) magnetization-field loops at 5 K for $x = 0.8-1.0$ and (inset) $x = 0.4-0.67$ samples.

In addition to the nuclear peaks, a series of strong magnetic diffraction peaks, indexed by a (1/2 1/2 1/2) propagation vector of the cubic cell, were observed in the Super-D2B neutron diffraction patterns of all the $Bi_xCa_{1-x}FeO_3$ samples. The magnetic intensities were unchanged between 10 K and room temperature, showing that the ordering temperatures are ≫300 K and that there are no structural or magnetic phase transitions over this interval. The magnetic peaks were fitted well by a G-type antiferromagnetic model in which each Fe moment is antiparallel to the six nearest neighbors. The moments are parallel to the *c*-axis in the rhombohedral phases and the refined magnitudes are shown in Table 1.

The high temperature evolution of the magnetic structures of the $Bi_xCa_{1-x}FeO_3$ perovskites has been investigated by temperature-dependent D1B neutron powder diffraction. The magnetic peak intensities decrease to zero at very similar Neel temperatures for all samples, $T_N = 350-370$ °C, as shown for $Bi_{0.67}Ca_{0.33}FeO_3$ in Figure 8. Figure 9 shows the temperature evolution of the magnetic moments across the series. The ordered magnetic moment decreases with decreasing x, from 4.1 μ_B at $x = 1$ to 3.6 μ_B at $x = 0.4$ (Table 1) but, the curvature and T_N values are remarkably constant across the $Bi_xCa_{1-x}FeO_3$ series. The moment reduction by 0.5 μ_B on going from $x = 1$ to $x = 0.4$ is close to the ideal change of 0.6 μ_B expected for the oxidation of $S = 5/2$ Fe^{3+} to high spin, $S = 2$, Fe^{4+}, and this provides indirect evidence that the oxygen content remains near-stoichiometric throughout.

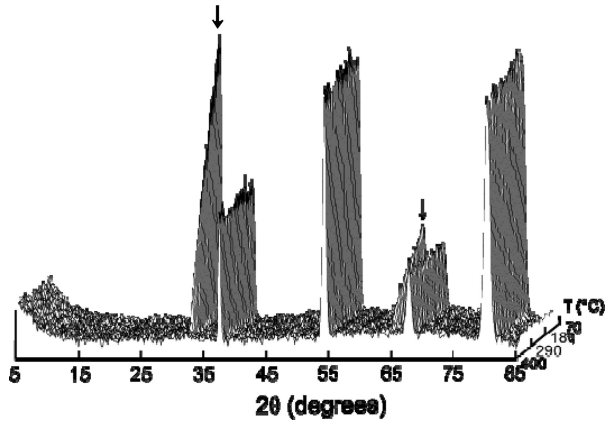

Figure 8. Temperature-dependent D1B neutron diffraction data for $Bi_{0.8}Ca_{0.2}FeO_3$ at 70−400 °C, with magnetic peaks marked by arrows.

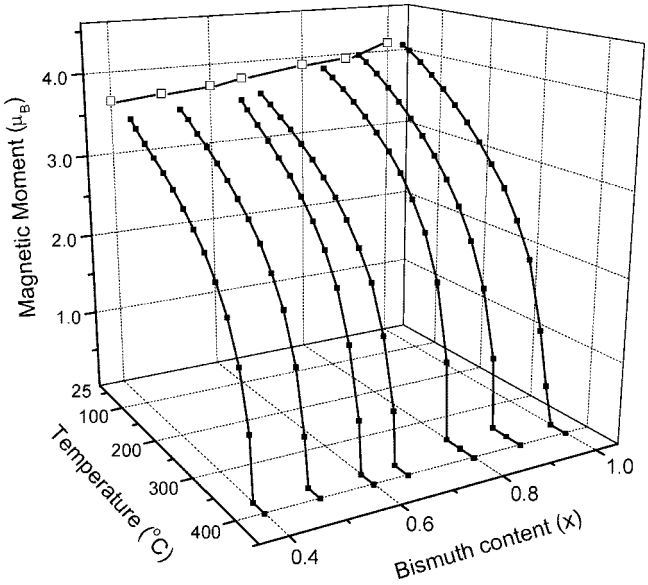

Figure 9. Evolution of magnetic moments in the $Bi_xCa_{1-x}FeO_3$ series as functions of x and temperature.

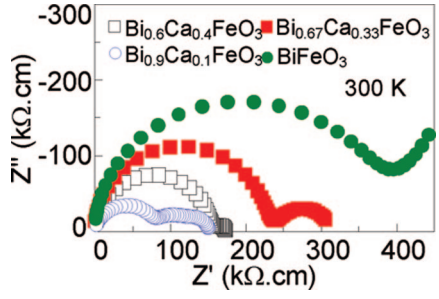

Figure 10. Impedance complex plane (Z^*) plots for representative $Bi_xCa_{1-x}FeO_3$ materials at 300 K.

3.5. Electronic Transport and Permittivity Measurements. All of the $Bi_xCa_{1-x}FeO_3$samples are insulating and behave as leaky dielectrics. The impedances of sintered pellets were investigated over a wide frequency range (1×10^0 to 1×10^6 Hz) between 10 and 320 K. The complex Z^* plane plots of 300 K impedance (Figure 10) reveal the presence of a large semicircular arc at high frequencies with an associated resistance of ∼50−500 kΩ cm and a capacitance of ∼ 2−5 pF cm^{-1}. This arc could be modeled on a single parallel resistor-capacitor (RC) element and the capacitance is consistent with a bulk (intragrain) response.[38] Arrhenius plots of these bulk conductivities for the $Bi_xCa_{1-x}FeO_3$ series are shown in Figure 11. All of the samples show a single activation energy over the measured temperature range. The monophasic cubic $x = 0.4-0.67$ samples show a consistent trend as bulk conductivity decreases with increasing x and the activation energy, E_a, increases as shown in Figure 12. However, the biphasic $x = 0.8$ and 0.9 samples do not follow this trend and have relatively high conductivities and lower activation energies. This suggests that the conductivity of the doped rhombohedral phase is higher than that of the cubic phase because of the high level of structural disorder in the latter.

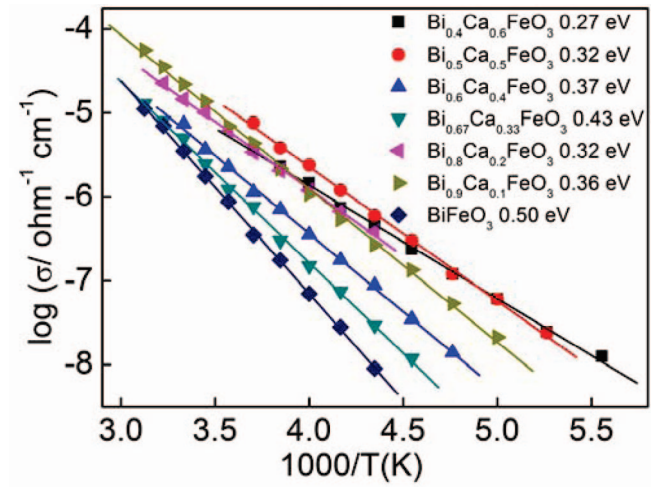

Figure 11. Arrhenius plots of the bulk component in the a.c. conductivity for the $Bi_xCa_{1-x}FeO_3$ series.

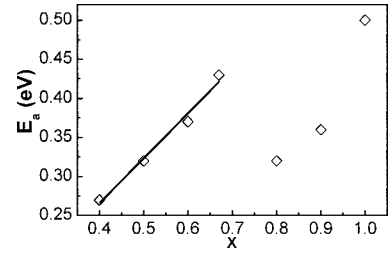

Figure 12. Variation in activation energy (from Figure 11) with Bi content x in the $Bi_xCa_{1-x}FeO_3$ series, with a linear fit in the $x = 0.4-0.67$ region.

The Z^* plots in Figure 10 also reveal the presence of a second, smaller arc at lower frequencies in all samples, except for $x = 0.9$ where two low-frequency arcs are observed. The magnitude of the low-frequency arc increased dramatically when the electrodes were changed from Au to InGa alloy, although the bulk response was unchanged, showing that the low-frequency arc is associated with a nonohmic contact between the metal electrode and these leaky dielectrics. This arises from a mismatch between the Fermi-energy level of the ceramics with the work function of the metal electrode. Identification of the further additional arc in $x = 0.9$ was not pursued but is most probably related

(38) Irvine, J. T. S.; Sinclair, D. C.; West, A. R. *Adv. Mater.* **1990**, *2*, 132–138.

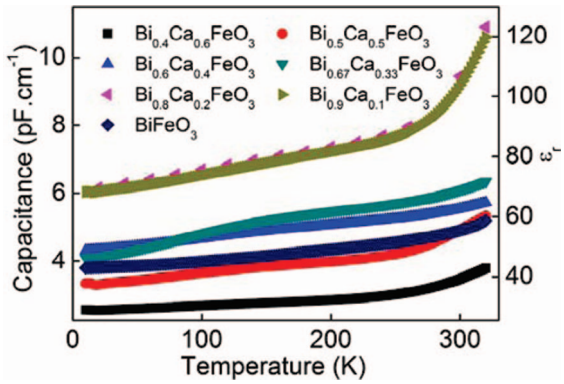

Figure 13. Permittivity versus temperature plots for the $Bi_xCa_{1-x}FeO_3$ series.

to the complex nature of this sample, which is poorly approximated even as a mixture of cubic and rhombohedral phases.

Similar trends are observed for the bulk permittivities of the $Bi_xCa_{1-x}FeO_3$ materials in Figure 13, which increase both with temperature and with x from 0.4 to 0.67 in the cubic regime. This is consistent with replacement of Ca^{2+} by the more polarizable Bi^{3+} ion on the A-site of the perovskite lattice. The biphasic $x = 0.8$ and 0.9 samples have almost identical, anomalously high permittivities; however, the relative permittivity of the $x = 1$ $BiFeO_3$ sample is lower than expected. This is probably related to the low ceramic density of the sample that was sintered at a significantly lower temperature than the other $Bi_xCa_{1-x}FeO_3$ samples.

4. Discussion

This investigation demonstrates that a wide range of $Bi_xCa_{1-x}FeO_3$ solid solutions ($x = 0.4-1$) can be synthesized in air by optimizing reaction temperatures for the various x compositions. At lower x values, mixtures of brownmillerite and perovskite phases are formed. Accurate oxygen analysis has not proved straightforward. Results of structure refinements suggest that the materials are near oxygen stoichiometric throughout but more precise control will be needed, in particular to tune dielectric properties.

The structural evolution of the $Bi_xCa_{1-x}FeO_3$ series appears straightforward based on standard laboratory X-ray diffractometry, with a transition from rhombohedral $R3c$ to cubic $Pm\bar{3}m$ symmetry as x decreases below ~0.8. However, the high resolution provided by synchrotron X-ray diffraction and the sensitivity of neutrons to oxygen displacements show that the structural transition and the cubic structure itself are more complex. Phase coexistence is observed in the $x = 0.8$ and 0.9 samples and is associated with enhanced magnetic and dielectric responses. A two-phase structural description works well for the $x = 0.8$ sample, but is more approximate for $x = 0.9$. This may reflect differences in their syntheses: the $x = 0.8$ sample was quenched, whereas $x = 0.9$ was slow-cooled, perhaps allowing a continuum of structures between rhombohedral and cubic to form. Substantial disordered displacements of Bi/Ca from the A-sites, and perpendicular shifts of the oxide anions are observed in all of the cubic $Bi_xCa_{1-x}FeO_3$ phases. The Fe−O distances decrease slightly from 2.01 to 1.99 Å as Fe is oxidized with decreasing x, and the Fe−O−Fe bridges are bent away from the ideal value of 180 to ~155°. The range of Bi/Ca−O distances in these disordered cubic models (typically 2.1−3.4 Å) is comparable to the distribution of Bi−O distances (2.26−3.46 Å) observed in the ordered rhombohedral structure of $BiFeO_3$ (Table 2), showing that local lone-pair distortions of Bi^{3+} are the likely cause of the disorder.

No long-range order of the local displacements is observed in the X-ray or neutron diffraction profiles of the cubic phases, even for $x = 0.67$, which was synthesized in case of any charge-ordering superstructure. However, HRTEM reveals well-defined microstructures in the two samples initially investigated ($x = 0.67$ and 0.8). The principal feature is a commensurate (q00) superstructure with q changing from 1/5 for $x = 0.67$ to $q = 1/8$ for $x = 0.8$, which commonly gives rise to domain structures. More complex microstructures are also observed for the $x = 0.8$, as this sample contains both bulk cubic and rhombohedral phases. Further work will be needed to characterize the local structures in the $Bi_xCa_{1-x}FeO_3$ series.

Doped $BiFeO_3$ materials are of particular interest for their multiferroic properties as $BiFeO_3$ is one of very few materials to show ferroelectric and magnetic ordering well above room temperature. Although $BiFeO_3$ has a modulated magnetic structure, a simple collinear antiferromagnetic arrangement is observed in the doped $Bi_xCa_{1-x}FeO_3$ materials. This suppression of the modulation is observed for many A site dopings including both isovalent (e.g., La^{3+}) and nonisovalent (Ca^{2+}, Sr^{2+}, Pb^{2+}) substitutions.[20,22,39−41] A surprising result is the robustness of the antiferromagnetic order in the $Bi_xCa_{1-x}FeO_3$ series. Replacing 60% of the Bi by Ca leads to only a slight decrease in the Neel temperature from 643 to 623 K, and the antiferromagnetically ordered room temperature moment decreases only as expected for the replacement of $S = 5/2$ Fe^{3+} by high-spin $S = 2$ Fe^{4+}. However, the ferroelectric order that accompanies the rhombohedral lattice distortion is rapidly suppressed through the formation of a disordered cubic structure, which is the only phase observed for $x < 0.8$. Phase coexistence is observed for $x = 0.8$ and 0.9, and the transformation of the quenched $x = 0.8$ sample to a completely rhombohedral phase in the high-temperature X-ray experiment demonstrates that the sample properties will be very sensitive to thermal treatments in the $x = 0.8-1.0$ range.

The present $Bi_xCa_{1-x}FeO_3$ samples are leaky dielectrics, with conductivity generally increasing with x, as expected for hole doping from the oxidation of Fe^{3+} to Fe^{4+}. Enhanced magnetizations and permittivities are observed for $x = 0.8-1.0$, in particular in the $x = 0.9$ sample. This shows an appreciable magnetic hysteresis (Figure 7b) although the loop collapses close to $H = 0$ suggesting that the induced magnetization is of metamagnetic rather

(39) Sosnowska, I.; Loewenhaupt, M.; David, W. I. F.; Ibberson, R. M. *Mater. Sci. Forum* **1993**, *133−136*, 683.
(40) Zhang, S.-T.; Zhang, Y.; Lu, M.-H.; Du, C.-L.; Chen, Y.-F.; Liu, Z.-G.; Zhu, Y.-Y.; Ming, N.-B.; Pan, X. Q. *Appl. Phys. Lett.* **2006**, *88*, 162901.
(41) Sosnowska, I.; Schäfer, W.; Kockelmann, W.; Andersen, K. H.; Troyanchuk, I. O. *Appl. Phys. A: Mater. Sci. Process.* **2002**, *74*, S1040.

than spontaneous origin. This sample and the $x = 0.8$ material have relative permittivities of ~100 at room temperature. The $x = 0.8-1.0$ region appears the most promising to investigate improved $BiFeO_3$-based multiferroics, but further work is needed to control the structures, microstructures, and oxygen content in this useful domain.

Acknowledgment. We thank Drs. A. Hewat and P. Henry; M. Brunelli, Dr. I. Margiolaki, and Dr. W. van Beek; and Mr. R. Blackley for assistance with data collection at ILL, ESRF, and the University of St. Andrews electron microscopy facility, respectively. We acknowledge EPSRC for provision of these facilities and for financial support.

CM8031048